

Non-Linear Hall Effect in Multi-Weyl Semimetals

Saswata Roy

Undergraduate Programme, Indian Institute of Science, Bangalore 560012, India

Awadhesh Narayan*

Solid State and Structural Chemistry Unit,

Indian Institute of Science, Bangalore 560012, India

(Dated: August 22, 2023)

Abstract

In the presence of time reversal symmetry, a non-linear Hall effect can occur in systems without an inversion symmetry. One of the prominent candidates for detection of such Hall signals are Weyl semimetals. In this article, we investigate the Berry curvature induced second and third order Hall effect in multi-Weyl semimetals with topological charges $n = 1, 2, 3$. We use low energy effective models to obtain general analytical expressions and discover the presence of a large Berry curvature dipole in multi-Weyl semimetals. We also study the Berry curvature dipole in a realistic tight-binding lattice model and observe two different kinds of variation with increasing topological charge – these can be attributed to different underlying Berry curvature components. We provide estimates of the signatures of second harmonic of Hall signal in multi-Weyl semimetals, which can be detected experimentally. Furthermore, we predict the existence of a third order Hall signal in multi-Weyl semimetals. We derive the analytical expressions of Berry connection polarizability tensor, which is responsible for third order effects, using a low energy model and estimate the measurable conductivity. Our work can help guide experimental discovery of Berry curvature multipole physics in multi-Weyl semimetals.

I. INTRODUCTION

A geometric phase may be acquired by a classical or quantum system when undergoing cyclic adiabatic processes. Independently discovered by Kato¹, Pancharatnam², and Longuet-Higgins *et al.*³, in different settings, the notion was organized in a general framework by Berry⁴. Berry's phase plays a key role in various condensed matter phenomena such as quantum Hall effect, spin hall effects, electric polarization and orbital magnetism⁵. Berry curvature, which originates from the Berry flux, acts as the magnetic field in the momentum space and is intimately connected to the celebrated quantum Hall effect⁶.

Recently, Sodemann and Fu, building on earlier work^{7,8}, have discovered the role of the *first order moment* of the Berry curvature – termed Berry curvature dipole (BCD) – in transport properties of quantum systems⁹. Surprisingly, BCD can lead to a non-linear Hall effect in time-reversal invariant systems⁹. The conventional Hall effect can be thought of as connected to the zeroth order moment of the Berry curvature while the first order moment leads to the second harmonic generation in the Hall signal^{10,11}. A growing number of generalizations to other non-linear phenomena have also been proposed^{12–26}. Similarly, higher order moments of the Berry curvature are predicted to produce higher harmonics of the Hall signal²⁷. To completely describe the third order conductivity tensor, another intrinsic band geometric quantity known as Berry connection polarizability (BCP) tensor has been proposed²⁸.

BCDs and the related non-linear Hall effect have been predicted for a spectrum of materials ranging from two-dimensional materials^{29–33}, tilted massive Dirac and Weyl cone systems^{34–36}, Weyl semimetals³⁷, large Rashba systems³⁸, and strained monolayer and bilayer graphene³⁹, to name just a few. In parallel to theoretical predictions, there have been noteworthy developments along the experimental front. Second order non-linear Hall effect was experimentally first observed in few layer transition metal dichalcogenide WTe₂^{40,41}. Following these pioneering reports, signatures of non-linear Hall signals have been detected in a growing number of materials, including Dirac semimetals⁴², Kondo materials⁴³, artificially corrugated bilayer graphene⁴⁴, monolayer WSe₂⁴⁵, twisted WSe₂⁴⁶, MoTe₂⁴⁷, organic Dirac materials⁴⁸, topological insulator surfaces⁴⁹ and Weyl semimetal TaIrTe₄⁵⁰. Very recently, third order non-linear signals have been experimentally detected in MoTe₂⁵¹.

An important class of materials for the realization of non-linear Hall effect are Weyl

semimetals – topological semimetallic systems exhibiting a Weyl fermion dispersion in the low energy regime^{52–54}. The point where two bands cross is known as the Weyl point. These points act as a source or sink of Berry curvature in momentum space and hence are associated with integer charged monopole and chirality. Weyl points with opposite chirality can merge and annihilate each other. On the other hand, Weyl nodes with same chirality can merge to form Weyl points with higher topological charge, which are named multi-Weyl semimetals. These systems are stabilised only when point group symmetry protects such a merging⁵⁵, hence there are discrete allowed values of topological charge, n ^{56,57}. Multi-Weyl semimetals have been predicted to show many interesting properties such as chiral effects, anomalous transport phenomena and distinct optical signatures^{58–72}.

Motivated by these exciting developments, here we study BCD in multi-Weyl semimetals using a low energy model, as well as a suitable tight-binding model. We obtain general analytical expressions (for arbitrary n) for the Berry curvature using the low energy model and discover the presence of a large BCD in multi-Weyl semimetals. To complement our analytical calculations, we next turn to a three dimensional tight-binding model and study the dependence of BCD on different model parameters for different monopole charges. In general, we find that a higher monopole charge facilitates higher magnitude of generated second harmonic of Hall signal. Further, we calculate the BCP tensor components for our low energy model and predict the existence of third-order Hall conductivity in multi-Weyl semimetals. For the existing symmetries in our system the third order contribution is less than that of second order contribution, but can be dominant if second order signal is suppressed. Our work can guide experimental discovery of Berry curvature multipole physics in multi-Weyl semimetals and also help to characterize new classes of multi-Weyl semimetal materials with higher topological charges.

II. BERRY CURVATURE, BERRY CURVATURE DIPOLE AND BERRY CONNECTION POLARIZABILITY TENSOR

Here we briefly review the notions of Berry curvature, its dipole (BCD) and BCP tensor, and their relation to transport properties. In response to an oscillating electric field, $\mathbf{E}(t) = \text{Re}[\boldsymbol{\varepsilon}e^{i\omega t}]$, a non-linear current, $J_a = \text{Re}[J_a^{(0)} + J_a^{(2)}e^{2i\omega t}]$ flows through the material with $J_a^{(0)} = \chi_{abc}^{(0)}\varepsilon_b\varepsilon_c^*$ and $J_a^{(2)} = \chi_{abc}^{(2)}\varepsilon_b\varepsilon_c$. In systems that preserve time-reversal symmetry the

coefficients are given by⁹

$$\chi_{abc}^{(0)} = \chi_{abc}^{(2)} = \frac{\epsilon^{acd} D_{bd} e^3 \tau}{2\hbar^2 (1 + i\omega t)}, \quad (1)$$

where ϵ^{acd} is the Levi-Civita symbol, τ is momentum relaxation time, ω is the frequency and $-e$ is the charge of electron. Here D_{bd} is the BCD, which is formulated as

$$D_{bd} = - \sum_i \int [d\mathbf{k}] \frac{\partial \epsilon_{\mathbf{k}}^i}{\partial k_b} \Omega_{i\mathbf{k}}^d \frac{\partial f_{\mathbf{k}}}{\partial \epsilon_{\mathbf{k}}^i}. \quad (2)$$

Here $a, b, c, d \in \{x, y, z\}$, $f_{\mathbf{k}}$ is the equilibrium Fermi-Dirac distribution, $\epsilon_{\mathbf{k}}^i$ is the energy of the i -th energy band and wavevector \mathbf{k} , $\Omega_{i\mathbf{k}}^d$ is the Berry curvature component in direction d for the i -th energy band and wave vector \mathbf{k} and $[d\mathbf{k}] = d^3\mathbf{k}/(2\pi)^3$. The Berry curvature, in turn, can be found as⁵

$$\Omega_{i\mathbf{k}}^a = -\epsilon^{abc} \text{Im} \sum_{j \neq i} \frac{\langle i | \frac{\partial H}{\partial k_b} | j \rangle \langle j | \frac{\partial H}{\partial k_c} | i \rangle - \langle i | \frac{\partial H}{\partial k_c} | j \rangle \langle j | \frac{\partial H}{\partial k_b} | i \rangle}{(\epsilon_{\mathbf{k}}^i - \epsilon_{\mathbf{k}}^j)^2}, \quad (3)$$

where $|i\rangle$ is an eigenstate of the Hamiltonian H that corresponds to band i with energy $\epsilon_{\mathbf{k}}^i$ for a wave vector \mathbf{k} . Notably, the integral in Equation 2 can survive in time-reversal symmetric systems, as long as the inversion symmetry is broken – this enables a finite Berry curvature to obtain a non-zero value of the BCD. We also define a BCD *density*³⁴

$$d_{bd}(\mathbf{k}) = (\partial_{\mathbf{k}}^b \epsilon_{\mathbf{k}}) \Omega_{\mathbf{k}}^d, \quad (4)$$

which is the kernel of the integral in Equation 2. As we will see, this quantity, d_{bd} gives further insights into the physics of the Berry curvature dipole.

Going beyond the second order, third order contributions to the Hall effect can be connected to the BCP tensor, which is an intrinsic band geometric quantity⁷³. It can be expressed in terms of the unperturbed eigenstates $|i\rangle$ and band energy ϵ_i as⁷³

$$G_{ab} = 2\text{Re} \sum_{i \neq j} \frac{(\mathcal{A}_a)_{ij} (\mathcal{A}_b)_{ij}}{\epsilon_i - \epsilon_j}. \quad (5)$$

where, \mathcal{A} is the Berry connection. The Berry curvature needs to be corrected to first order in presence of an external electric field

$$\tilde{\Omega}(\mathbf{k}) = \Omega(\mathbf{k}) + \Omega^{(1)}(\mathbf{k}), \quad (6)$$

which is given by

$$\boldsymbol{\Omega}^{(1)} = \nabla_{\mathbf{k}} \times \boldsymbol{\mathcal{A}}^{(1)}. \quad (7)$$

In turn, the first order correction of Berry connection, $\boldsymbol{\mathcal{A}}^{(1)}$, is related to the BCP tensor as

$$\mathcal{A}_a^{(1)}(\mathbf{k}) = G_{ab}(\mathbf{k})E_b. \quad (8)$$

Using Equations 6 and 8, we can also define a Berry curvature polarizability as

$$P_{ab} = \frac{\partial \tilde{\Omega}_a}{\partial E_b} = \epsilon_{acd} \partial_c G_{db}. \quad (9)$$

Using the components of the BCP tensor, we can calculate the third order conductivity tensor χ that follows $j_a^{(3)} = \chi_{abcd} E_b E_c E_d$, with Einstein summation convention assumed. Further, χ can be broken into two parts – χ^I which is linear in τ and χ^{II} which is proportional to τ^3 .

$$\chi_{abcd}^I = \tau \left[2 \int [d\mathbf{k}] (\partial_a \partial_b G_{cd}) f_{\mathbf{k}} - \int [d\mathbf{k}] (\partial_c \partial_d G_{ab}) f_{\mathbf{k}} - \frac{1}{2} \int [d\mathbf{k}] (v_a v_b G_{cd}) f_{\mathbf{k}}'' \right], \quad (10a)$$

$$\chi_{abcd}^{II} = -\tau^3 \int [d\mathbf{k}] v_a \partial_b \partial_c \partial_d f_{\mathbf{k}}. \quad (10b)$$

Here $v_i = \frac{\partial E}{\partial k_i}$ and χ_{abcd}^I is the major contributor to the third order non-linear Hall response as it has a linear dependence on the relaxation time τ .

III. RESULTS AND DISCUSSION

A. Low-energy model

We begin with a low energy model Hamiltonian^{74,75} that describes the multi-Weyl semimetals effectively. Setting $\hbar = 1$, the Hamiltonian reads

$$H = C_s(k_y - sQ)\mathbb{I} + s\alpha \boldsymbol{\sigma} \cdot \mathbf{n}_{\mathbf{k}}, \quad (11)$$

where $\mathbf{n}_{\mathbf{k}} = [k_{\perp}^n \cos(n\phi), k_{\perp}^n \sin(n\phi), v_z(k_z - sQ)/\alpha]$, $k_{\perp} = \sqrt{k_x^2 + k_y^2}$, $\boldsymbol{\sigma} = (\sigma_x, \sigma_y, \sigma_z)$ is the triad of Pauli matrices, $s = \pm 1$ characterizes the chirality of the Weyl point, \mathbb{I} is the

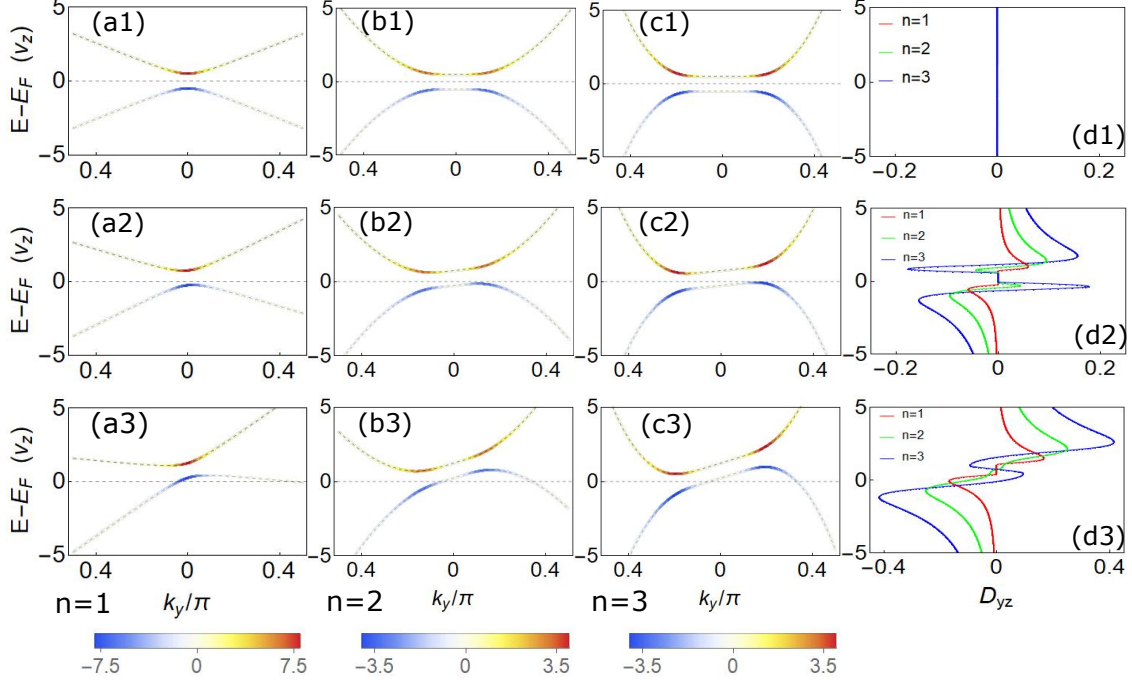


FIG. 1. **Band structure, Berry curvature and Berry curvature dipole in multi-Weyl semimetals.** Band structures of the low energy Hamiltonian with tilt for multi-Weyl semimetals along k_y (setting $k_x = k_z = 0$) with the following choice of parameters (a1) $n = 1$, $C_s = 0$, (a2) $n = 1$, $C_s = 0.5$, (a3) $n = 1$, $C_s = 1.5$, (b1) $n = 2$, $C_s = 0$, (b2) $n = 2$, $C_s = 0.5$, (b3) $n = 2$, $C_s = 1.5$, (c1) $n = 3$, $C_s = 0$, (c2) $n = 3$, $C_s = 0.5$, (c3) $n = 3$, $C_s = 1.5$. Value of the Berry curvature is superimposed on the band structure and corresponding color scales are shown. The Berry curvature is concentrated close to the multi-Weyl nodes, with opposite values for conduction and valence bands. (d1-d3) Berry curvature dipole for the corresponding tilt (C_s) values with $n = 1$ in red, $n = 2$ in green and $n = 3$ in blue. Berry curvature dipole becomes non-zero only when a tilt is introduced, as expected. Note the increase in dipole with increasing topological charge. The maximum value of dipole is observed in the vicinity of the energy where Berry curvature is most concentrated and this maximum value increases with an increase in C_s . Other parameters common to all plots are $v_z = 1$, $\alpha = 2$, $s = -1$, and $Q = 0.5$.

identity matrix, C_s is the tilt parameter, and $\phi = \tan^{-1}(k_y/k_x)$. Here α generalizes the Fermi velocity in k_x - k_y plane and is a dimensionless quantity (in our chosen units). The multi-Weyl nodes are separated by $2Q$ along the k_z direction. v_z acts as the Fermi velocity. Finally, n is the monopole charge associated with the node. The dispersion relation for this

model is given by

$$E_{\pm}(\mathbf{k}) = C_s(k_y - sQ) \pm \sqrt{(k_z - sQ)^2 v_z^2 + \alpha^2(k_x^2 + k_y^2)^n}. \quad (12)$$

Note the power dependence on n with varying k_x and k_y – near the Weyl point the energy bands follow a linear, quadratic and cubic behaviour, respectively, for $n = 1, 2$ and 3 . The parameter C_s controls the tilt along k_y direction. We have consistently used $s = -1$ and $Q = 0.5$ in this article. For these particular parameter values the bands will touch each other at $(0, 0, -0.5)$ point in the momentum space.

We begin our analysis by deriving analytical expressions for Berry curvature for general topological charge n . Using Equations 3, 11, 12 we calculate the Berry curvature components along the three directions. These read

$$\Omega_{\mp}^x = \pm \frac{nv_z k_x \alpha^2 (k_x^2 + k_y^2)^{n-1}}{2s[(k_z - sQ)^2 v_z^2 + \alpha^2(k_x^2 + k_y^2)^n]^{\frac{3}{2}}}, \quad (13a)$$

$$\Omega_{\mp}^y = \mp \frac{nv_z k_y \alpha^2 (k_x^2 + k_y^2)^{n-1}}{2s[(k_z - sQ)^2 v_z^2 + \alpha^2(k_x^2 + k_y^2)^n]^{\frac{3}{2}}}, \quad (13b)$$

$$\Omega_{\mp}^z = \pm \frac{\alpha^2 n^2 (k_z - sQ) s v_z (k_x^2 + k_y^2)^{n-1}}{2[(k_z - sQ)^2 v_z^2 + \alpha^2(k_x^2 + k_y^2)^n]^{\frac{3}{2}}}. \quad (13c)$$

It is worth noting that, Ω_z has n^2 dependence compared to the n dependence in Ω_x and Ω_y . This plays a key role in determining relative magnitudes of different BCD components. Also note that these expressions reduce to the expected ones for $n = 1$, i.e., the usual Weyl semimetal case.

The band dispersions along k_y (for $k_x = k_z = 0$), with the value of the z component of the Berry curvature superimposed on them for various tilt values are plotted in Fig. 1. We note that the Berry curvature is opposite for the valence and conduction bands. In case of no tilt ($C_s = 0$), the inversion symmetry of the system is not broken and hence in a time-reversal symmetric system, such as ours, there is no Berry dipole. This can be attributed to the symmetric distribution of Berry curvature near the band edges. With the introduction of tilt along the k_y direction, the inversion symmetry is broken and Berry curvature is now asymmetric at the band edges for all values of topological charge n . Hence peaks in the BCD appear, as shown in Fig. 1(d2)-(d3). We find that the maxima of the BCD is not

exactly at the same energy where the Berry curvature is concentrated as the group velocity ($\frac{\partial E}{\partial k_y}$) vanishes at that point. So, an optimal energy where the product of group velocity and Berry curvature is maximum gives the maximum value of the dipole. As we will show, this optimal energy window can be investigated by analysis of the BCD density, as defined in Equation 4. Because of the absence of carriers in the band gap, the BCD is zero for energies within the gap. However, with larger tilts, a finite density of carriers is present invariably at all energy values for higher order band crossings and hence a non-zero BCD is found at all energies (except precisely at the band touching point). This can be seen clearly from Fig.1(d3). However, for the Weyl semimetal with topological charge $n = 1$, there is always a zero BCD within the band gap. For higher order band crossings, Berry curvature is concentrated further away from the Brillouin zone centre (i.e., $k_y = 0$) and the group velocity ($\frac{\partial E}{\partial k_y}$) is also higher near those points owing to the higher order dispersion. As a result, we discover that the BCD is highest for the case of $n = 3$, followed by $n = 2$ and 1. With further increase in tilt, the bands have an even more asymmetric distribution of Berry curvature and larger group velocities, which lead to further increase in the magnitude of BCD. Other than D_{yz} , only the D_{zy} component is non-zero amongst the off-diagonal ones in the BCD tensor. This component is smaller than the D_{yz} component but follows a similar distribution where increasing tilt increases the magnitude of BCD.

To gain further insights into the nature of the BCD in multi-Weyl semimetals, we next turn to the BCD density. In Fig. 2, the dipole density, d_{yz} , as defined by Equation 4 are plotted for all three values of n . When tilt is zero the distribution of dipole density is symmetric in a $k_x - k_y$ plane for all values of k_z and n , hence cancels out to give a net zero contribution to BCD, as we present in Fig. 2(a). As we introduce a finite tilt, the dipole density distribution becomes asymmetric and gives a contribution from all $k_x - k_y$ planes which is seen in Fig. 2(b). We also note that the positive and negative values of d_{yz} are also different, thereby resulting in a finite net value. We also find that the extremum points in the dipole density distribution are close to the multi-Weyl nodes. On the other hand, the points in the momentum plane which are away from multi-Weyl points contribute little to the BCD. For $n = 3$, dipole density is highest in magnitude and has a larger momentum space spread as well. As a result, $n = 3$ multi-Weyl semimetal produces the highest BCD. In the case of $n = 1$, maximum value of dipole density is higher but it spans a very small momentum region, when compared to $n = 2$ and $n = 3$. So, the total BCD value for $n = 2$

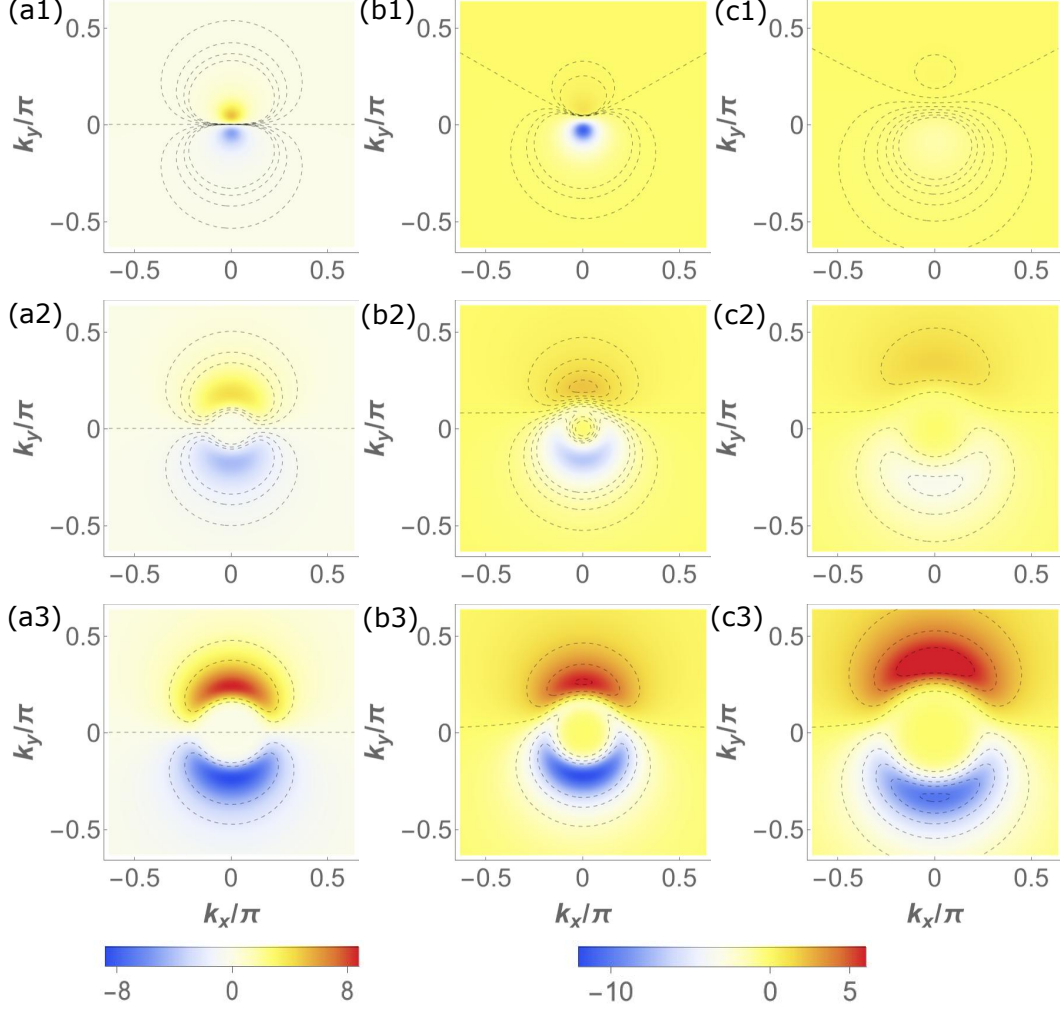


FIG. 2. **Berry curvature dipole densities with tilt.** Berry curvature dipole densities plotted in the $k_x - k_y$ plane (setting $k_z = 0$) for (a1) $n = 1$, $C_s = 0$, (a2) $n = 2$, $C_s = 0$, (a3) $n = 3$, $C_s = 0$, (b1) $n = 1$, $C_s = 1$, (b2) $n = 2$, $C_s = 1$, (b3) $n = 3$, $C_s = 1$. For plots (c1)-(c3) we set $k_z = 1$ for (c1) $n = 1$, $C_s = 1$, (c2) $n = 2$, $C_s = 1$, and (c3) $n = 3$, $C_s = 1$. Color scale for panels (b) and (c) are kept same for a better comparison. Dashed lines are contours for dipole density values close to zero. The distribution of dipole densities is anti-symmetric along k_y for zero tilt and hence no net Berry curvature dipole is obtained. With the introduction of tilt this exact anti-symmetry disappears and as a result finite dipole originates. As we go further away from $k_z = 0$, the dipole density declines and spreads out suggesting a lower contribution to Berry curvature dipole from $k_x - k_y$ planes further away. Other parameters are $s = -1$, $Q = 0.5$, $v_z = 1$, $\alpha = 2$.

surpasses that of $n = 1$, which produces the BCD variation that we show in Fig. 1. The BCD densities in Fig. 2(c) are plotted for the same tilt as Fig. 2(b), but for $k_z = 1$ which is located further away from the location of the multi-Weyl points. We observe that the dipole density reduces. This decrease in dipole density is specially pronounced for $n = 1$ and $n = 2$, as shown in Fig. 2(c).

It is worth noting here that the dipole density, d_{yz} , is an odd function of k_z , while d_{zy} is an odd function of k_y for each of the bands for a three-dimensional material. So, the full three-dimensional integral will lead to net zero off-diagonal components of the BCD for this model, which is consistent with the recent findings of Ref. 76. However, as the authors have pointed out, this is not the case for many real materials and first-principles calculations show a high value of off-diagonal components of BCD in Weyl semimetal materials³⁷. Thus, low energy models are insufficient to provide complete details of BCD in three-dimensional systems. However, as we have seen, they can help in understanding the general trends and their origin from two-dimensional subsystems. To get a complete understanding of BCD in multi-Weyl semimetals, we move on to tight-binding models in the next section, which can provide a more realistic description of real materials.

B. Tight-binding model

Motivated by the intriguing behavior of BCD in low energy models of multi-Weyl semimetals, we next study a lattice model for these systems. The tight-binding Hamiltonian reads⁷⁷

$$H^n = d_0^n + \mathbf{d}^n \cdot \boldsymbol{\sigma}, \quad (14)$$

where $\boldsymbol{\sigma} = (\sigma_x, \sigma_y, \sigma_z)$ are the Pauli matrices, d_0^n and \mathbf{d}^n are lattice periodic functions and n is the topological charge of the multi-Weyl semimetal. The following parameters control the behaviour of the Hamiltonian: t_C represents the tilt of the Weyl spectrum, while t and t_z are the hopping strengths. The lattice constant is taken to be unity. The components of $D^n = [d_0^n, \mathbf{d}^n]$ for $n = 1, 2, 3$ are the following

$$D^1 = [t_C(\cos k_z + \cos k_x - 1), t \sin k_x, t \sin k_y, t_z \cos k_z], \quad (15a)$$

$$D^2 = [t_C(\cos k_z + \cos k_x - 1), t(\cos k_x - \cos k_y), 2t \sin k_x \sin k_y, t_z \cos k_z], \quad (15b)$$

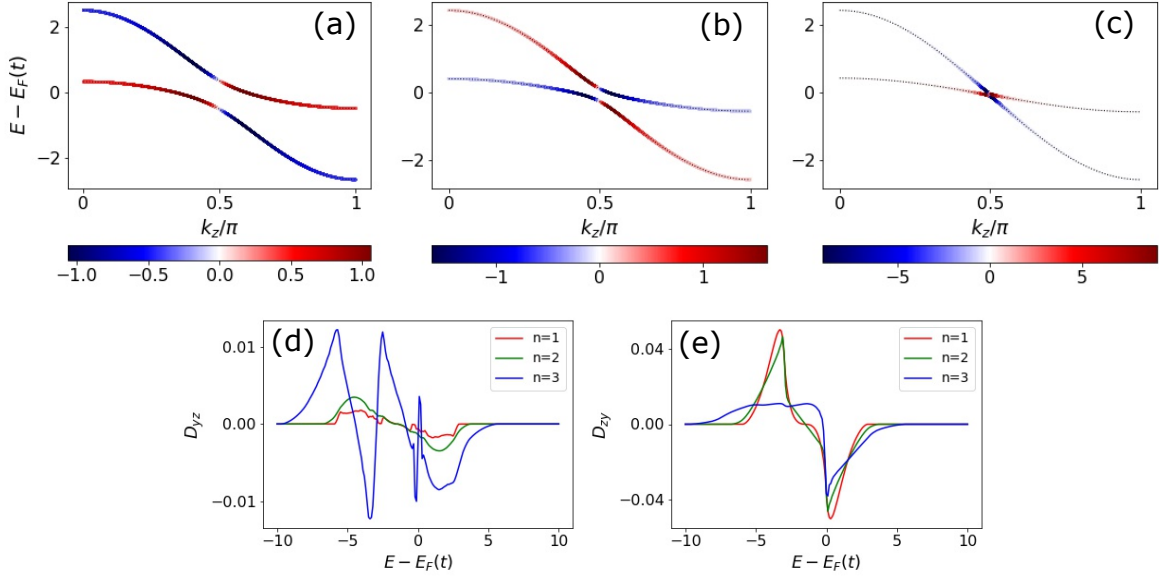


FIG. 3. **Band structure, Berry curvature and Berry curvature dipole for lattice models of multi-Weyl semimetals.** Band structure with the values of Berry curvature superimposed on it is plotted for the lattice Hamiltonian along k_z direction with $k_y = 0.1\pi$ and $k_x = 0.1\pi$ for (a) $n = 1$, (b) $n = 2$, (c) $n = 3$. Note the largest values of Berry curvature for highest topological charge $n = 3$. Non-zero Berry curvature dipole components (d) D_{yz} and (e) D_{zy} are plotted for the same parameters. Relative peak values of Berry curvature dipole for $n = 1, 2, 3$ match our predictions from the low-energy model for the D_{yz} component. However, for the D_{zy} component we observe a different trend because, for this case, the dominant factor for determining magnitude of Berry dipole is the y component of the Berry curvature, which follows a different dependence on the topological charge. Other parameters are chosen to be $t_C = 1.5$, $t = 1$ and $t_z = 1$.

$$D^3 = [t_C(\cos k_z + \cos k_x - 1), t \sin k_x(1 - \cos k_x - 3(1 - \cos k_y)), -t \sin k_y(1 - \cos k_y - 3(1 - \cos k_x)), t_z \cos k_z]. \quad (15c)$$

In all the three cases the Weyl points are found at $(0, 0, \pm\pi/2)$. The magnitude of the tilt (t_C) determines whether the system is a type-I or a type-II Weyl semimetal. The dispersion relations for the different topological charge n are as follows

$$E_{\pm}^{n=1} = t_C(\cos k_x + \cos k_z - 1) \pm [(t^2(2 - \cos 2k_x - \cos 2k_y) + t_z^2(1 + \cos 2k_z))/2]^{1/2}, \quad (16a)$$

$$E_{\pm}^{n=2} = t_C(\cos k_x + \cos k_z - 1) \pm [(t^2(4 - \cos 2k_x - \cos 2k_y + \cos(2(k_x + k_y)) + \cos(2(k_x - k_y)) - 2(\cos k_x - k_y + \cos(k_x + k_y))) + t_z^2(\cos 2k_z + 1))/2]^{1/2}, \quad (16b)$$

$$E_{\pm}^{n=3} = t_C(\cos k_x + \cos k_z - 1) \pm [t^2((\sin k_x(1 - \cos k_x - 3(1 - \cos k_y)))^2 + (-t \sin k_y(1 - \cos k_y - 3(1 - \cos k_x)))^2) + (t_z \cos k_z)^2]^{1/2}. \quad (16c)$$

For our numerical computations using the above tight-binding models, we employ the PythTB⁷⁸ code to generate the lattice system. Then we use the Wannier-Berri package^{79,80} for calculating the band structures, densities of states, Berry curvature and BCD. For the calculation of BCD a $100 \times 100 \times 100$ k -grid was used and convergence was checked.

We begin our investigation by examining the band structures for different multi-Weyl systems, as shown in Fig. 3(a)-(c) along k_z with $k_x = k_y = 0.1\pi$. The superimposed values of Berry curvature confirm that the Berry curvature is indeed concentrated near the Weyl points. The z component of the Berry curvature is highest in magnitude for $n = 3$ by some margin, which is the case for our low energy model as well. Further, the Berry curvature is opposite in sign for valence and conduction bands and also changes sign at the point at which the bands nearly touch.

The Hamiltonian described above has certain symmetry features that are important to understand which components of BCD will be non-zero. First of all it is time-reversal symmetric. Note that in this case anti-Hermitian complex conjugation is the time reversal operator. Inversion symmetry is broken for this system. It has mirror symmetries along k_y and k_z . In presence of these mirror symmetries⁹, only two components of BCD are expected to be non-zero, D_{yz} and D_{zy} , and this is confirmed by our numerical calculations.

The two non-zero components for all three topological charges are plotted in Fig.3(d)-(e). The two components have an opposite relative magnitude of peaks of Berry dipole for the three topological charges. For D_{yz} , highest magnitude is observed for $n = 3$, whereas magnitude is highest for $n = 1$ for D_{zy} component. These differences occur because of the difference in origin of the BCD in these two cases. For D_{yz} the involved Berry curvature component is Ω_z , which is perpendicular to the $k_x - k_y$ planes, in which multi-Weyl dispersion properties are present in our model. In other words, Ω_z is directly sensitive to the multi-Weyl nature of the dispersion as well as the higher topological charge. Besides Ω_z , the group velocity plays a major role in determining the magnitude of Berry dipole here. It is different for the three topological charges and largest for $n = 3$, again owing to the different

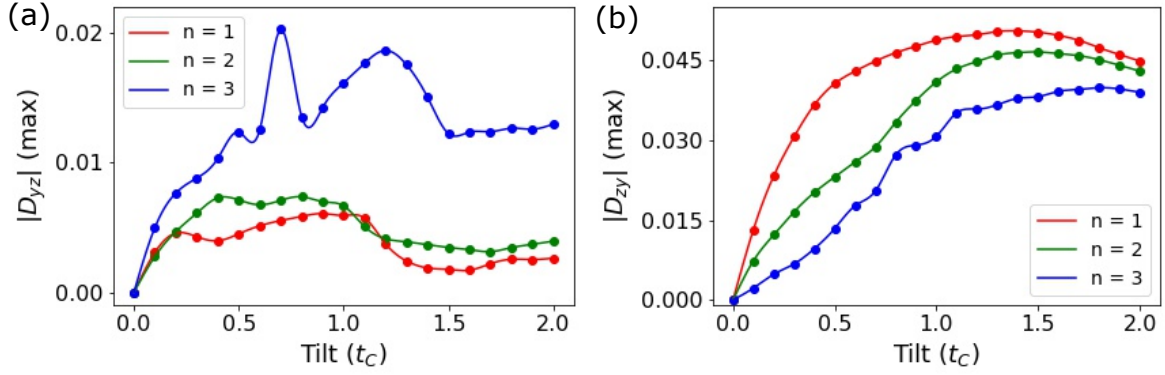


FIG. 4. **Maximum of Berry curvature dipole with tilt parameter.** Variation of maximum magnitude of Berry curvature dipole component (a) D_{yz} and (b) D_{zy} with tilt (t_C) for the lattice models of multi-Weyl semimetals for $n = 1, 2$ and 3 . The maximum of Berry curvature dipole variation with tilt is different for the two components. However, both components start to saturate after a certain tilt value. This indicates that several factors come in play in determining the magnitude of Berry curvature dipole in multi-Weyl semimetals. Other fixed parameters are $t = 1$ and $t_z = 1$.

dispersion. On the other hand, for D_{zy} , the relevant Berry curvature component is Ω_y , which decreases with increase in topological charge. Since the σ_x and σ_y coefficients of Hamiltonian change for the three topological charges, behaviour of Ω_y is different than Ω_z . This plays the major role in determining the BCD magnitude, as the relevant group velocity (v_z) is the same for all three values of n . Thus we uncover an unexpected variation in BCD sign and magnitude with topological charge, depending on the tensor component. In Fig. 4(a), we plot the variation of the maximum of D_{yz} with tilt and observe that for topological charge $n = 3$, the dipole is greatest in magnitude for all tilt values. Topological charges $n = 1$ and $n = 2$ are close in value to each other. On the other hand, for D_{zy} component, shown in Fig. 4(b), we find that $n = 1$ has the highest maximum BCD for all tilt values followed by $n = 2$ and $n = 3$. Our striking prediction of this anisotropy in the BCD should be directly verifiable in non-linear Hall measurements, as we will discuss later.

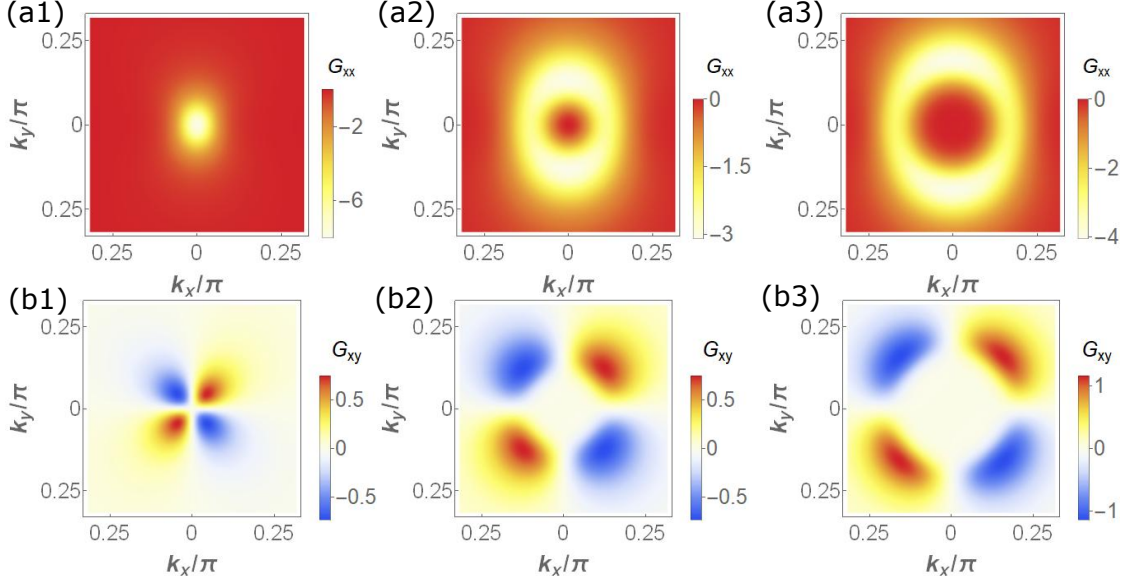


FIG. 5. **Berry connection polarizability tensor components.** Distribution of Berry curvature polarizability tensor components in the $k_x - k_y$ plane. Here G_{xx} is plotted for (a1) $n = 1$, (a2) $n = 2$, (a3) $n = 3$, and G_{xy} is shown for (b1) $n = 1$, (b2) $n = 2$, (b3) $n = 3$ for $s = -1$, $Q = 0.5$ and $k_z = 0$. These are independent of the tilt of the system. Here G_{xx} behaves like a monopole, while G_{xy} exhibits a quadrupole-like pattern. Magnitudes of both components are peaked at positions where the Berry curvature peaks, i.e., where the band gap is minimal.

IV. THIRD ORDER HALL RESPONSE

After studying the second order non-linear Hall response in multi-Weyl semimetals, a natural question arises: can these systems show a higher order Hall response? To answer this question, we next investigate the third order Hall response in these systems. As we discussed before, the third order Hall response can be understood in the framework of the BCP tensor^{28,51}. We begin by deriving analytical expressions for the BCP components, for a general n , using our low energy Hamiltonian (see Equation 11). Using Equation 9, we find that the components of BCP are as follows

$$G_{xx} = -\frac{n^2 \alpha^2 (k_x^2 + k_y^2)^{n-2} [k_x^2 k_z^2 v_z^2 + k_y^2 (k_z^2 v_z^2 + (k_x^2 + k_y^2)^n \alpha^2)]}{4[k_z^2 v_z^2 + (k_x^2 + k_y^2)^n \alpha^2]^{5/2}}, \quad (17a)$$

$$G_{yy} = -\frac{n^2 \alpha^2 (k_x^2 + k_y^2)^{n-2} [k_y^2 k_z^2 v_z^2 + k_x^2 (k_z^2 v_z^2 + (k_x^2 + k_y^2)^n \alpha^2)]}{4[k_z^2 v_z^2 + (k_x^2 + k_y^2)^n \alpha^2]^{5/2}}, \quad (17b)$$

$$G_{zz} = -\frac{v_z^2 \alpha^2 (k_x^2 + k_y^2)^n}{4[k_z^2 v_z^2 + (k_x^2 + k_y^2)^n \alpha^2]^{5/2}}, \quad (17c)$$

$$G_{xy} = G_{yx} = \frac{n^2 k_x k_y \alpha^4 (k_x^2 + k_y^2)^{2(n-1)}}{4[k_z^2 v_z^2 + (k_x^2 + k_y^2)^n \alpha^2]^{5/2}}, \quad (17d)$$

$$G_{xz} = G_{zx} = \frac{k_x k_z n v_z^2 \alpha^2 (k_x^2 + k_y^2)^{(n-1)}}{4[k_z^2 v_z^2 + (k_x^2 + k_y^2)^n \alpha^2]^{5/2}}, \quad (17e)$$

$$G_{yz} = G_{zy} = \frac{k_y k_z n v_z^2 \alpha^2 (k_x^2 + k_y^2)^{(n-1)}}{4[k_z^2 v_z^2 + (k_x^2 + k_y^2)^n \alpha^2]^{5/2}}. \quad (17f)$$

Note that all nine components of the BCP tensor are, in general, non-zero for multi-Weyl semimetals and depend on the topological charge n . Further, the off-diagonal components are symmetric, i.e., $G_{xy} = G_{yx}$, $G_{xz} = G_{zx}$, and $G_{yz} = G_{zy}$. In Fig. 5, we plot the different representative components of the BCP tensor in the $k_x - k_y$ plane. We notice several interesting features of the BCP tensor. The diagonal components G_{xx} and G_{yy} behave like a monopole for topological charge $n = 1$ and are peaked at $k_x = k_y = 0$, i.e., where the band gap is minimal. For topological charges $n = 2$ and 3 , these components still behave like a monopole, but are not peaked at the origin, but rather at a position slightly away from it. These peaks are in the same momentum region where the Berry curvature shows peaks for the corresponding topological charge, i.e., where the band gaps are minimal. Strikingly, the off-diagonal component, G_{xy} , has a quadrupole-like structure and shows a similar peak behaviour, where the peaks move further from $k_x = k_y = 0$ with increase in the topological charge.

Calculating the full conductivity tensor analytically for a three-dimensional material is a formidable task with many components of G and χ contributing to it and leading to cumbersome expressions. Rather, to gain more insight, we calculate the conductivity tensor for the special case considering $k_z = 0$. For simplifying the symmetry discussions, we assume $Q = 0$. In this case, the multi-Weyl points are located on the mirror line $M_x = \sigma_x$, such that $M_x H(k_x, k_y) M_x^{-1} = H(-k_x, k_y)$. When the applied electric field is along or perpendicular to this mirror line, there will not be any third order Hall current generated. This means that χ_{yyyy} , χ_{xxxy} and other such permutations with three y and one x components or three x and one y components will be zero and will not contribute to the conductivity tensor. On the other hand, an in-plane electric field, defined as $\mathbf{E} = E(\cos \theta, \sin \theta)$ will produce a third order response $j_H^{(3)} = \mathbf{j}^{(3)} \cdot \hat{\mathbf{n}}$, where $\hat{\mathbf{n}} = (-\sin \theta, \cos \theta)$ is the normal to \mathbf{E} . The third order contribution to the Hall conductivity is then determined by the conductivity

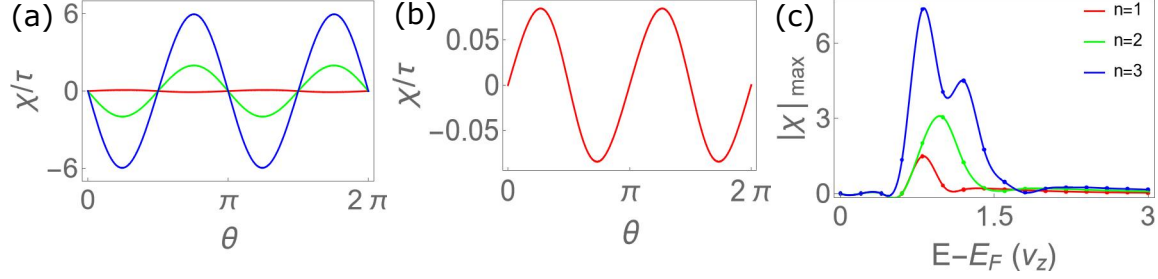


FIG. 6. **Third order conductivity tensor for multi-Weyl semimetals.** Angular dependence of the third order conductivity tensor. The different curves are for $n = 1$ (red), $n = 2$ (green) and $n = 3$ (blue). (b) Zoomed-in plot of the curve for $n = 1$ in panel (a). Third order conductivity increases substantially with increasing monopole charge. (c) The variation of the maximum conductivity with energy. It is near zero at very low and high Fermi energies and peaks at a moderate Fermi energy similar to the Berry curvature dipole distribution. Other parameters are chosen to be $C_s = 0.5$, $v_z = 1$, $\alpha = 2$, $s = -1$, $Q = 0.5$, $E - E_F = 1.1$, and $k_z = 0$.

tensor $\chi_H = \frac{j_H^{(3)}}{E^3}$. For our system, with the prescribed symmetries we find the third order conductivity tensor as

$$\chi_H(\theta) = (-\chi_{11} + 3\chi_{21}) \sin^3 \theta \cos \theta + (\chi_{22} - 3\chi_{12}) \sin \theta \cos^3 \theta, \quad (18)$$

where θ is measured from the mirror line, and the shorthand notations stand for $\chi_{11} = \chi_{xxxx}$, $\chi_{22} = \chi_{yyyy}$, $\chi_{12} = (\chi_{xxyy} + \chi_{xyxy} + \chi_{xyyx})/3$ and $\chi_{21} = (\chi_{yyxx} + \chi_{yxyx} + \chi_{yxxy})/3$. We have evaluated the third order conductivity tensor numerically for different multi-Weyl semimetals and the results are shown in Fig. 6. For the special case of no tilt, χ_H is zero for all values of θ due to symmetry reasons discussed above. For a finite tilt, we observe a non-zero value of the conductivity tensor and the sign for $n = 1$ is opposite to the cases of $n = 2$ and $n = 3$. Remarkably, we find that the magnitude of χ is highest for $n = 3$ followed by $n = 2$ and $n = 1$. This is due to higher group velocity, less symmetry and sharper features in G_{ab} for higher topological charges. For all values of topological charge, χ_H varies with the direction of applied field (i.e., with θ) with a periodicity of π . It vanishes when θ is a multiple of $\pi/2$, which is consistent with our symmetry analysis. In Fig. 6(c), we have presented the maximum value of the conductivity tensor with the Fermi energy. It turns out to show a variation similar to the BCD, where there is a peak at moderate Fermi energy

but becomes nearly zero at higher and lower values of Fermi energy. Further, multi-Weyl semimetals with $n = 3$ have the highest third order response followed by $n = 2$ and $n = 1$. Therefore, our calculations show that multi-Weyl semimetals with higher topological charges can be suitable platforms for observing enhanced higher order Hall response.

V. EXPERIMENTAL CONSIDERATIONS

Here, we estimate the magnitude of second order non-linear Hall response that can be measured in experiments. First, we need to calculate the conductivity tensors in Equation 1. In typical experimental setups^{40,41}, the relaxation time, τ , is of the order of picoseconds and the ac frequency can be varied between 10-1000 Hz. So, the frequency dependence in denominator can be neglected as $\omega\tau \ll 1$. Using these values, the non zero components of the conductivity tensor are

$$\chi_{xyy} = -\chi_{yyx} = 0.1846D_{yz}, \quad (19a)$$

$$\chi_{xzz} = -\chi_{zzx} = -0.1846D_{zy}. \quad (19b)$$

Using the previously mentioned relation, $J_a^{2\omega} = \chi_{abc}E_bE_c$, we can find the second order Hall current. For simplicity, we consider three cases where the current is confined in a cartesian plane, namely xy , yz or zx . This gives us the following expressions for the current

$$J_y^{2\omega} = \chi_{yyx}E_yE_x \quad \text{when} \quad \mathbf{E} = (E_x, E_y, 0), \quad (20a)$$

$$J_x^{2\omega} = \chi_{xyy}E_y^2 + \chi_{xzz}E_z^2 \quad \text{when} \quad \mathbf{E} = (0, E_y, E_z), \quad (20b)$$

$$J_z^{2\omega} = \chi_{zzx}E_zE_x \quad \text{when} \quad \mathbf{E} = (E_x, 0, E_z). \quad (20c)$$

Consider a typical sample dimension to be $10 \times 6 \times 2 \mu\text{m}^3$ and the resistivity to be isotropic in all directions such that $\rho_x = \rho_y = \rho_z = 50 \mu\Omega\text{cm}$. Let us consider $V_x = 1 \text{ V}$ and $V_y = 1 \text{ V}$. This choice gives us the current density, $J_y^{2\omega} = -0.1846D_{yz}\frac{V_yV_x}{L_xL_y} = -3.077 \times 10^9 D_{yz} \text{ A/m}^2$. This, in turn, produces a voltage, $V_y^{2\omega} = -1.8462 \times 10^4 \rho_y D_{yz} \text{ V}$. Therefore, we obtain the ratio to be $\frac{V_y^{2\omega}}{(V_x^\omega)^2} = -9.231 \times 10^{-3} D_{yz} \text{ V}^{-1}$. This ratio is $16.3 \times 10^{-6} \text{ V}^{-1}$ for $n = 1$, $31.9 \times 10^{-6} \text{ V}^{-1}$ for $n = 2$, and $112.8 \times 10^{-6} \text{ V}^{-1}$ for $n = 3$. These are well within the reach of current experimental techniques and can clearly distinguish our proposal of topological charge dependence of the non-linear Hall signal. It can also be noted that, for the typical

parameters we used, the current $J_x^{2\omega}$ (Equation 20b), will have a overall higher magnitude of response. The above discussion also makes it clear that we can orient the applied electric fields to measure second harmonics that are dependent only on one of the BCD components or both the components.

VI. SUMMARY AND OUTLOOK

In summary, we studied Berry curvature multipole physics in multi-Weyl semimetals. Using a low-energy model, we calculated the general expressions for Berry curvature and its dependence on topological charge, n . We discovered the occurrence of Berry curvature dipole in multi-Weyl semimetals. Our low-energy model predicted a general trend of increasing BCD magnitude with topological charge. With inspiration from low-energy model results, we used a tight-binding lattice model to study the dipole in a more realistic setting. We found two different variations in the its components with topological charges. While one component (D_{yz}) increases with topological charge the other one (D_{zy}) decreases with it. From studying their origins, we concluded that the magnitude of the Berry curvature dipole depends on size of the involved Berry curvature component (which, in turn, is dependent on the topological charge), the extent to which it is distributed in the momentum space and the group velocity of the relevant bands. Further, we analytically obtained the Berry connection polarizability tensor – responsible for the third harmonic generation of the Hall signal – for a low energy model and found all its components to be non-zero in multi-Weyl semimetals. We calculated the third order conductivity and showed that its magnitude increases with the underlying topological charge. We hope that our work can motivate exploration of Berry curvature multipole physics in multi-Weyl semimetals and help in characterizing new classes of multi-Weyl semimetal materials with higher topological charges.

ACKNOWLEDGMENTS

We acknowledge useful discussions with N. B. Joseph, D. Varghese, A Bandyopadhyay, H. Liu, S. A. Yang, S. Bhowal and N. A. Spaldin. S. R. thanks the Kishore Vaigyanik Pratishthan Yojana (KVPY) for a fellowship. A. N. acknowledges support from the startup grant of the Indian Institute of Science (SG/MHRD-19-0001) and DST-SERB (project number

* awadhesh@iisc.ac.in

- ¹ T. Kato, Journal of the Physical Society of Japan **5**, 435 (1950).
- ² S. Pancharatnam, in *Proceedings of the Indian Academy of Sciences-Section A*, Vol. 44 (Springer, 1956) pp. 398–417.
- ³ H. C. Longuet-Higgins, U. Öpik, M. H. L. Pryce, and R. Sack, Proceedings of the Royal Society of London. Series A. Mathematical and Physical Sciences **244**, 1 (1958).
- ⁴ M. V. Berry, Proceedings of the Royal Society of London. A. Mathematical and Physical Sciences **392**, 45 (1984).
- ⁵ D. Xiao, M.-C. Chang, and Q. Niu, Rev. Mod. Phys. **82**, 1959 (2010).
- ⁶ D. J. Thouless, M. Kohmoto, M. P. Nightingale, and M. den Nijs, Phys. Rev. Lett. **49**, 405 (1982).
- ⁷ E. Deyo, L. Golub, E. Ivchenko, and B. Spivak, arXiv preprint arXiv:0904.1917 (2009).
- ⁸ J. E. Moore and J. Orenstein, Physical review letters **105**, 026805 (2010).
- ⁹ I. Sodemann and L. Fu, Phys. Rev. Lett. **115**, 216806 (2015).
- ¹⁰ Z. Du, H.-Z. Lu, and X. Xie, arXiv preprint arXiv:2105.10940 (2021).
- ¹¹ C. Ortix, arXiv preprint arXiv:2104.06690 (2021).
- ¹² K. Hamamoto, M. Ezawa, K. W. Kim, T. Morimoto, and N. Nagaosa, Physical Review B **95**, 224430 (2017).
- ¹³ Y. Araki, Scientific reports **8**, 1 (2018).
- ¹⁴ E. König, M. Dzero, A. Levchenko, and D. Pesin, Physical Review B **99**, 155404 (2019).
- ¹⁵ M. Papaj and L. Fu, Physical review letters **123**, 216802 (2019).
- ¹⁶ X.-Q. Yu, Z.-G. Zhu, J.-S. You, T. Low, and G. Su, Physical Review B **99**, 201410 (2019).
- ¹⁷ C. Zeng, S. Nandy, A. Taraphder, and S. Tewari, Physical Review B **100**, 245102 (2019).
- ¹⁸ D. Mandal, K. Das, and A. Agarwal, Physical Review B **102**, 205414 (2020).
- ¹⁹ R. Nakai and N. Nagaosa, Physical Review B **99**, 115201 (2019).
- ²⁰ C. Zeng, S. Nandy, and S. Tewari, Physical Review Research **2**, 032066 (2020).
- ²¹ S. K. Das, T. Nag, and S. Nandy, Phys. Rev. B **104**, 115420 (2021).
- ²² S. Nandy and I. Sodemann, Phys. Rev. B **100**, 195117 (2019).

- ²³ Z. Du, C. Wang, S. Li, H.-Z. Lu, and X. Xie, *Nature communications* **10**, 1 (2019).
- ²⁴ Z. Du, C. Wang, H.-P. Sun, H.-Z. Lu, and X. Xie, *Nature communications* **12**, 1 (2021).
- ²⁵ C. Xiao, Z. Du, and Q. Niu, *Physical Review B* **100**, 165422 (2019).
- ²⁶ R. Resta, arXiv preprint arXiv:2101.10949 (2021).
- ²⁷ C.-P. Zhang, X.-J. Gao, Y.-M. Xie, H. C. Po, and K. T. Law, arXiv preprint arXiv:2012.15628 (2020).
- ²⁸ H. Liu, J. Zhao, Y. Huang, X. Feng, X. Cong, W. Wu, S. Lai, W.-b. Gao, and S. A. Yang, arXiv preprint arXiv:2106.04931 (2021).
- ²⁹ T. Low, Y. Jiang, and F. Guinea, *Physical Review B* **92**, 235447 (2015).
- ³⁰ J.-S. You, S. Fang, S.-Y. Xu, E. Kaxiras, and T. Low, *Phys. Rev. B* **98**, 121109 (2018).
- ³¹ Y. Zhang, J. van den Brink, C. Felser, and B. Yan, *2D Materials* **5**, 044001 (2018).
- ³² N. B. Joseph and A. Narayan, *Journal of Physics: Condensed Matter* **33**, 465001 (2021).
- ³³ S. S. Samal, S. Nandy, and K. Saha, *Physical Review B* **103**, L201202 (2021).
- ³⁴ Z. Z. Du, C. M. Wang, H.-Z. Lu, and X. C. Xie, *Phys. Rev. Lett.* **121**, 266601 (2018).
- ³⁵ R.-C. Xiao, D.-F. Shao, W. Huang, and H. Jiang, *Physical Review B* **102**, 024109 (2020).
- ³⁶ S. Singh, J. Kim, K. M. Rabe, and D. Vanderbilt, *Physical review letters* **125**, 046402 (2020).
- ³⁷ Y. Zhang, Y. Sun, and B. Yan, *Physical Review B* **97**, 041101 (2018).
- ³⁸ J. I. Facio, D. Efremov, K. Koepernik, J.-S. You, I. Sodemann, and J. Van den Brink, *Physical review letters* **121**, 246403 (2018).
- ³⁹ R. Battilomo, N. Scopigno, and C. Ortix, *Phys. Rev. Lett.* **123**, 196403 (2019).
- ⁴⁰ Q. Ma, S.-Y. Xu, H. Shen, D. MacNeill, V. Fatemi, T.-R. Chang, A. M. Mier Valdivia, S. Wu, Z. Du, C.-H. Hsu, S. Fang, Q. D. Gibson, K. Watanabe, T. Taniguchi, R. J. Cava, E. Kaxiras, H.-Z. Lu, H. Lin, L. Fu, N. Gedik, and P. Jarillo-Herrero, *Nature* **565**, 337 (2019).
- ⁴¹ K. Kang, T. Li, E. Sohn, J. Shan, and K. F. Mak, *Nature materials* **18**, 324 (2019).
- ⁴² O. O. Shvetsov, V. D. Esin, A. V. Timonina, N. N. Kolesnikov, and E. Deviatov, *JETP Letters* **109**, 715 (2019).
- ⁴³ S. Dzsaber, X. Yan, M. Taupin, G. Eguchi, A. Prokofiev, T. Shiroka, P. Blaha, O. Rubel, S. E. Grefe, H.-H. Lai, *et al.*, *Proceedings of the National Academy of Sciences* **118** (2021).
- ⁴⁴ S.-C. Ho, C.-H. Chang, Y.-C. Hsieh, S.-T. Lo, B. Huang, T.-H.-Y. Vu, C. Ortix, and T.-M. Chen, *Nature Electronics* **4**, 116 (2021).

- ⁴⁵ M.-S. Qin, P.-F. Zhu, X.-G. Ye, W.-Z. Xu, Z.-H. Song, J. Liang, K. Liu, and Z.-M. Liao, Chinese Physics Letters **38**, 017301 (2021).
- ⁴⁶ M. Huang, Z. Wu, J. Hu, X. Cai, E. Li, L. An, X. Feng, Z. Ye, N. Lin, K. T. Law, *et al.*, arXiv preprint arXiv:2006.05615 (2020).
- ⁴⁷ A. Tiwari, F. Chen, S. Zhong, E. Drueke, J. Koo, A. Kaczmarek, C. Xiao, J. Gao, X. Luo, Q. Niu, *et al.*, Nature communications **12**, 1 (2021).
- ⁴⁸ A. Kiswandhi and T. Osada, arXiv preprint arXiv:2103.00300 (2021).
- ⁴⁹ P. He, H. Isobe, D. Zhu, C.-H. Hsu, L. Fu, and H. Yang, Nature communications **12**, 1 (2021).
- ⁵⁰ D. Kumar, C.-H. Hsu, R. Sharma, T.-R. Chang, P. Yu, J. Wang, G. Eda, G. Liang, and H. Yang, Nature Nanotechnology **16**, 421 (2021).
- ⁵¹ S. Lai, H. Liu, Z. Zhang, J. Zhao, X. Feng, N. Wang, C. Tang, Y. Liu, K. S. Novoselov, S. A. Yang, and W.-b. Gao, Nature Nanotechnology **16**, 869 (2021).
- ⁵² S. Rao, arXiv preprint arXiv:1603.02821 (2016).
- ⁵³ B. Yan and C. Felser, Annual Review of Condensed Matter Physics **8**, 337 (2017).
- ⁵⁴ N. Armitage, E. Mele, and A. Vishwanath, Reviews of Modern Physics **90**, 015001 (2018).
- ⁵⁵ C. Fang, M. J. Gilbert, X. Dai, and B. A. Bernevig, Phys. Rev. Lett. **108**, 266802 (2012).
- ⁵⁶ S.-M. Huang, S.-Y. Xu, I. Belopolski, C.-C. Lee, G. Chang, T.-R. Chang, B. Wang, N. Alidoust, G. Bian, M. Neupane, *et al.*, Proceedings of the National Academy of Sciences **113**, 1180 (2016).
- ⁵⁷ G. Xu, H. Weng, Z. Wang, X. Dai, and Z. Fang, Physical review letters **107**, 186806 (2011).
- ⁵⁸ S. Ahn, E. Mele, and H. Min, Physical Review B **95**, 161112 (2017).
- ⁵⁹ S. Ahn, E. Hwang, and H. Min, Scientific reports **6**, 1 (2016).
- ⁶⁰ D. Sinha and K. Sengupta, Physical Review B **99**, 075153 (2019).
- ⁶¹ K. Kulikov, D. Sinha, Y. M. Shukrinov, and K. Sengupta, Physical Review B **101**, 075110 (2020).
- ⁶² S. Park, S. Woo, E. Mele, and H. Min, Physical Review B **95**, 161113 (2017).
- ⁶³ Z.-M. Huang, J. Zhou, and S.-Q. Shen, Physical Review B **96**, 085201 (2017).
- ⁶⁴ R. M. Dantas, F. Peña-Benitez, B. Roy, and P. Surówka, Physical Review Research **2**, 013007 (2020).
- ⁶⁵ H.-F. Lü, Y.-H. Deng, S.-S. Ke, Y. Guo, and H.-W. Zhang, Physical Review B **99**, 115109 (2019).
- ⁶⁶ E. Gorbar, V. Miransky, I. Shovkovy, and P. Sukhachov, Physical Review B **96**, 155138 (2017).

- ⁶⁷ S. Mukherjee and J. Carbotte, Physical Review B **97**, 045150 (2018).
- ⁶⁸ Y. Sun and A. Wang, Journal of Physics: Condensed Matter **29**, 435306 (2017).
- ⁶⁹ R. Soto-Garrido, E. Muñoz, and V. Juričić, Physical Review Research **2**, 012043 (2020).
- ⁷⁰ D. Chowdhury, A. Banerjee, and A. Narayan, Physical Review A **103**, L051101 (2021).
- ⁷¹ J.-R. Wang, G.-Z. Liu, and C.-J. Zhang, Physical Review B **96**, 165142 (2017).
- ⁷² T. Nag, A. Menon, and B. Basu, Physical Review B **102**, 014307 (2020).
- ⁷³ H. Liu, J. Zhao, Y. Huang, X. Feng, C. Xiao, W. Wu, S. Lai, W. bo Gao, and S. A. Yang,
<http://arxiv.org/abs/2106.04931v2>.
- ⁷⁴ R. M. A. Dantas, F. Peña-Benitez, B. Roy, and P. Surówka, Journal of High Energy Physics **2018**, 69 (2018).
- ⁷⁵ A. Menon and B. Basu, Journal of Physics: Condensed Matter **33**, 045602 (2020).
- ⁷⁶ C. Zeng, S. Nandy, and S. Tewari, Phys. Rev. B **103**, 245119 (2021).
- ⁷⁷ A. Menon, S. Chattopadhyay, and B. Basu, Phys. Rev. B **104**, 075129 (2021).
- ⁷⁸ “Pythtb code,” <http://www.physics.rutgers.edu/pythtb/>, accessed: 2021-07-31.
- ⁷⁹ S. S. Tsirkin, npj Computational Materials **7**, 33 (2021).
- ⁸⁰ D. Destraz, L. Das, S. S. Tsirkin, Y. Xu, T. Neupert, J. Chang, A. Schilling, A. G. Grushin,
J. Kohlbrecher, L. Keller, P. Puphal, E. Pomjakushina, and J. S. White, npj Quantum Materials **5**, 5 (2020).